Editors' Suggestion

Variable chemical decoration of extended defects in Cu-poor $Cu_2ZnSnSe_4$ thin films

Torsten Schwarz,[1,*] Alex Redinger,[2] Susanne Siebentritt,[2] Zirong Peng,[1] Baptiste Gault,[1] Dierk Raabe,[1] and Pyuck-Pa Choi[3,†]

[1]*Max-Planck-Institut für Eisenforschung GmbH, Max-Planck-Straβe 1, 40237 Düsseldorf, Germany*

[2]*Laboratory for Photovoltaics, Physics and Materials Science Research Unit, University of Luxembourg, Belvaux, L-4422, Luxembourg*

[3]*Korea Advanced Institute of Science and Technology (KAIST), Daejeon 305-338, Republic of Korea*

(Received 15 October 2018; revised manuscript received 14 February 2019; published 19 March 2019)

We report on atom probe tomography studies of variable chemical decorations at extended defects in Cu-poor and Zn-rich $Cu_2ZnSnSe_4$ thin films. For a precursor film, which was co-evaporated at 320 °C, grain boundaries and dislocations are found enriched with Cu. Furthermore, Na out-diffusion from the soda-lime glass substrate occurs even at such a low temperature, resulting in Na segregation at defects. In contrast, stacking faults in the precursor film show clear Zn enrichment as well as Cu and Sn depletion. After an annealing step at 500 °C, we detect changes in the chemical composition of grain boundaries as compared to the precursor. Moreover, we measure an increase in the grain boundary excess of Na by one order of magnitude. We show that grain boundaries and dislocations in the annealed $Cu_2ZnSnSe_4$ film exhibit no or only slight variations in composition of the matrix elements. Thus, the effect of annealing is a homogenization of the chemical composition.

DOI: 10.1103/PhysRevMaterials.3.035402

I. INTRODUCTION

In recent years, the quest for novel absorber materials for thin-film solar cells has focused on the kesterite-structured semiconductors $Cu_2ZnSn(S, Se)_4$ (CZTS(e)) [1–3]. These compounds have numerous benefits such as direct band gaps, which can be tuned by the S/Se ratio from 1.0 eV to 1.5 eV [3], and high absorption coefficients ($\sim 10^4\,cm^{-1}$) for the solar spectral range, resulting in reduced material consumption and costs. Furthermore, CZTS(e) is composed of earth-abundant and nontoxic elements in contrast to In-containing $Cu(In, Ga)(S, Se)_2$ and Pb-containing halide perovskites. The current certified record efficiency of CZTS(e)-based solar cells is 12.6% [4], while for a small-area device an efficiency of even 13.8% [5] was reported.

A key factor usually limiting the performance of CZTS(e)-based solar cells is a deficit in the open-circuit voltage V_{OC} [1]. Since CZTS(e) absorber films are polycrystalline, extended defects such as grain boundaries (GBs), stacking faults (SFs), and dislocations may significantly alter the optoelectronic properties of the absorber [6–9]. Deep levels in the band gap known as Shockley-Read-Hall nonradiative recombination centers may be created by these extended defects and may thus lead to a reduced V_{OC}. Chemical fluctuations at such defects can also cause band bending and affect the charge carrier transport. Moreover, impurities can segregate at extended defects and may passivate or create deep defects.

Despite their large potential impact on the electrical properties of the absorber material, extended defects in CZTS(e) have not yet been systematically studied with respect to their chemical compositions. Cu-enriched GBs have been identified for Cu-poor and Zn-rich grown CZTS(e) films by energy-dispersive x-ray spectroscopy (EDX) and electron energy loss spectroscopy (EELS) measurements in a scanning transmission electron microscope (STEM) [10–13]. Detection of impurities of low compositions is challenging for these techniques and, therefore, in this work we have performed atom probe tomography (APT) studies on extended defects in CZTSe films. APT has demonstrated to be a powerful technique to trace the spatial distribution of impurities in CZTS(e) films [14–17]. The films studied here were grown under Cu-poor and Zn-rich growth conditions to suppress the formation of detrimental compounds such as $Cu_{2-x}Se$, Cu_2SnSe_3, and SnSe. The chosen growth conditions yielded outstanding cell efficiencies, i.e., $\geqslant$10% [13,18–22]. We measure changes in compositional trends of CZTSe GBs in a low-temperature (320 °C) grown CZTSe precursor film as compared to the final absorber obtained after annealing at 500 °C. We reveal that not only GBs but also SFs and dislocations can have variable chemical decorations and discuss possible effects of the observed compositional phenomena on the cell properties.

II. EXPERIMENT

The CZTS(e) films studied in this work were grown by a sequential process. Precursors were fabricated in a molecular beam epitaxy system by co-evaporation of Cu, Zn, Sn, and Se under Cu-poor ($[Cu]/([Zn] + [Sn]) < 1$) and Zn-rich ($[Zn]/[Sn] > 1$) conditions onto a Mo-coated soda-lime glass (SLG) substrate at 320 °C. In order to obtain an absorber, the precursor was subsequently annealed in a tube furnace at 500 °C for 30 min in a Se and SnSe atmosphere. More details on the specific film growth conditions can be found in Ref. [23]. For current-voltage (I-V) measurements, complete cells were fabricated out of the precursor and absorber by depositing a CdS buffer layer by chemical-bath deposition as well as by magnetron sputtering of i-ZnO and Al-doped ZnO and electron-beam evaporation of a Ni-Al grid. A sketch of

*schwarz@mpie.de
†p.choi@kaist.ac.kr

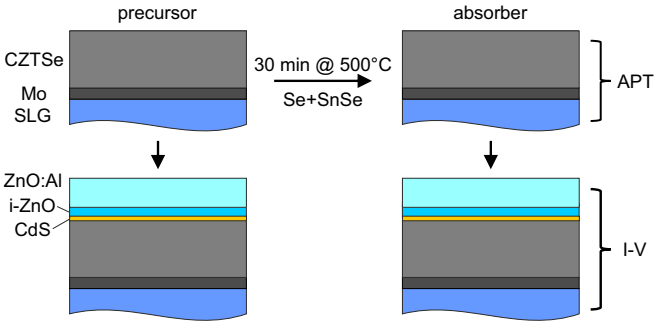

FIG. 1. Schematic presentation of the investigated samples. APT measurements were carried out on samples without having CdS/i-ZnO/ZnO:Al layers. The Ni-Al grid is not shown here.

the processing conditions for the samples used for APT and *I-V* measurements, respectively, is shown in Fig. 1.

The preparation of needle-shaped APT specimens was carried out using a dual-beam focused-ion-beam (FIB) (FEI Helios Nanolab 600i) system, following the protocol outlined in Ref. [24]. The lift-out regions for the APT specimen preparation were chosen randomly on the samples close to the surface of the CZTS(e) film, where the *pn* junction of the solar cell is formed. The analyses direction is parallel to the film-growth direction. To minimize Ga ion-induced damage, e.g., Cu out-diffusion [25], a 16 keV Ga beam and a low-energy (2–5 keV) Ga beam was used for coarse and final shaping of the APT specimens, respectively. APT analyses were performed using a local electrode atom probe (LEAP 5000XS, Cameca Instruments) at a specimen base temperature of 50 K. Measurements were done in pulsed laser mode, using a laser wavelength of 355 nm, ∼10 ps pulse length, an energy of 5 pJ, a repetition rate of 200 kHz, and an average detection rate of 10 ions per 1000 pulses.

III. RESULTS

A. Distribution of secondary phases and solar cell efficiency

The precursor synthesized in this work was Cu-poor ($[Cu]/([Zn]+[Sn]) < 1$) and Zn-rich ($[Zn]/[Sn] > 1$), as confirmed by EDX [23]. We did not detect $Cu_{2-x}Se$, Cu_2SnSe_3, and SnSe in our APT datasets. The excess Zn was found to lead to the formation of a complex nanoscaled ZnSe network across the entire film [16]. After annealing, the composition as well as the distribution of ZnSe remained unchanged [16].

Preparation of a solar cell, using the Cu-poor precursor film, yields zero efficiency. Possible reasons are the presence of deep defects such as Sn_{Zn}, which can be harmful if their concentration exceeds $>10^{10}\,cm^{-3}$ [26], and the presence of Cu-enriched GBs (see discussion) [14]. Since the precursor was grown at low temperature, one may also have a mixture of kesterite and stannite structured CZTSe, which cannot be distinguished by APT. Stannite inclusions can reduce the open-circuit voltage due to their smaller band gap compared to the kesterite matrix [3].

In order to yield working solar cells, an additional annealing step of the Cu-poor precursor is needed. The device made from this particular annealed precursor (absorber) gave an efficiency of 3.4%. Similar Cu-poor precursors led to higher efficiencies of up to 6% [23,27]. This is likely due to an improved quality of the interface, i.e., less defects, between the absorber and the CdS layer originating from a cleaning of the CZTS(e) surface with potassium cyanide (KCN) prior to annealing [23]. Since the dominant recombination path for Se-based devices is located in the bulk [27], we focus in the following on chemical fluctuations in the bulk.

B. Chemical fluctuations at CZTSe grain boundaries

Figures 2(a)–2(d) show three-dimensional maps of Na atoms acquired from the Cu-poor precursor before annealing. The blue isocomposition surfaces of 24.8 at. % Cu in Figs. 2(a) and 2(d) mark CZTSe GBs. ZnSe inclusions formed due to Zn excess during the growth were detected in other APT measurements of the precursor, but they are not shown here (more details are given in Ref. [16]). The composition profiles across the GBs labelled I and II along the red arrows shown in Figs. 2(b) and 2(d) are plotted in Figs. 2(e) and 2(f). Both profiles clearly show Cu enrichments at the GBs and slight depletions of Zn, Sn, and Se. Absolute compositions of Zn, Sn, and Se do not fluctuate as clearly as for Cu. Thus, Figs. 2(g) and 2(h) show the relative composition fluctuations c_{rel} across the GBs I and II, respectively, which are calculated as follows:

$$c_{rel} = {}^{c_i}\!/_{\bar{c}_i}\,, \tag{1}$$

where c_i is the composition of element i in each bin of the composition profile and $\bar{c}_i$ is the elemental composition averaged over the entire profile. Hence, the values of c_{rel} for elemental depletions and enrichments at GBs are <1 and >1, respectively. Zn and Sn depletions at the two GBs in Figs. 2(g) and 2(h) are clearly visible in the relative composition profiles. Also, slight depletion of Se can be seen at both GBs. Na atoms are segregated at the GBs or form clusters. Na compositions at GBs are $\leqslant$0.05 at. %, as shown in Figs. 2(e) and 2(f). For quantification of GB segregation of impurities, Gibbsian interfacial excess values have been determined from ladder diagrams. Latter diagrams are cumulative plots of the number of impurity atoms against the total number of atoms [28].

The Na excess values Γ_{Na} for the GBs I and II are 0.04 atoms/nm^2 and 0.03 atoms/nm^2, respectively. Changes in matrix element compositions and Na excess values of all analyzed GBs in the Cu-poor precursor are summarized in Table I. The average Na excess amounts to 0.05 ± 0.025 atoms/nm^2. In general, we observe for all GBs of the precursor a Cu enrichment and Zn, Sn, and Se depletion. The Na composition in Na clusters varies between 1.4 at.% and 2.5 at.%.

Figures 3(a)–3(c) show three-dimensional maps of Na acquired from the annealed Cu-poor absorber. Gray isocomposition surfaces of 32.0 at.% Zn mark ZnSe precipitates, which are usually observed in CTZSe films grown under Zn-rich conditions [29]. We observe several GBs decorated by Na as well as chemical fluctuations at GBs, which differ from those in the precursor. The composition profile in Fig. 3(d) across the GB VII reveals a significantly larger Na composition of ∼1.0 at.% than the average Na composition of ∼0.05 at.% at GBs in the precursor. Furthermore, co-segregation of K is

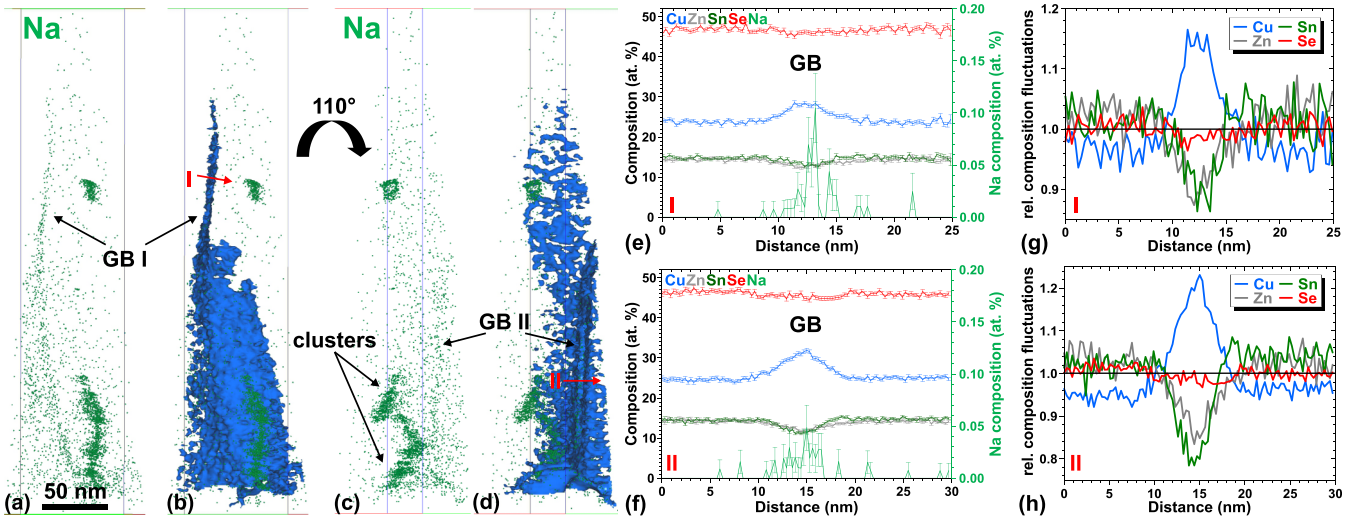

FIG. 2. (a)–(d) Three-dimensional elemental maps of Na (green) atoms from a dataset of the Cu-poor precursor. (c) and (d) are rotated by 110° with respect to (a) and (b). The blue isocomposition surfaces in (b) and (d) mark 24.8 at.% Cu and, hence, Cu-enriched CZTSe GBs. (e), (f) Composition profiles across the GBs I and II, i.e., along the red arrows given in (b) and (d), respectively. (g) and (h) show the calculated relative composition fluctuations of the composition profiles given in (e) and (f), respectively. To view the rotating elemental maps, see the Supplemental Material [48].

observed, where the determined excess values for Na and K are 1.27 atoms/nm^2 and 0.18 atoms/nm^2, respectively.

From Fig. 3(d), we also detect a slight Sn depletion at GB VII, whereas fluctuations of the other matrix elements at the GB are not clearly discernible. The relative composition profiles shown in Fig. 3(e) reveal a depletion of Zn at GB VII beside Sn depletion and a slight enrichment of Cu and Se. At another GB (VIII), Se enrichment and Zn depletion are more pronounced than at GB VII [see Fig. 3(f)], whereas Cu and Sn do not show any compositional fluctuations (not shown here). Furthermore, Fig. 3(f) also reveals a slightly higher Zn composition in one grain than in the adjacent grain. In contrast to GBs VII and VIII, GB IX, which is also decorated by Na, does not show any compositional fluctuations of the matrix elements [see Fig. 3(g)].

TABLE I. Chemical composition changes of the matrix elements at CZTSe GBs. +, −, o correspond to enrichment, depletion, and no change, respectively. P stands for precursor and A for absorber.

GB	Cu	Zn	Sn	Se	Γ_{Na} (atoms/nm^2)	Γ_K (atoms/nm^2)	Sample
I	++	−	−	−	0.04	−	P
II	++	−	−	−	0.03	−	P
III	+	−	−	−	0.09	−	P
IV	++	−	−	−	0.02	−	P
V	++	−−	−	−	0.06	−	P
VI	++	−	−	o	0.06	−	P
VII	+	−	−	+	1.27	0.18	A
VIII	o	−	o	+	0.27	0.11	A
IX	o	o	o	o	0.26	0.05	A
X	o	−	o	+	0.23	0.18	A
XI	−	−	o	+	0.46	0.10	A
XII	o	−	o	(+)	0.55	0.12	A
XIII	o	o	o	o	0.32	0.16	A
XIV	o	o	o	o	0.33	0.11	A
XV	o	o	o	o	0.19	−	A
XVI	+	(−)	−	o	1.10	0.13	A
XVII	o	−	o	o	0.41	0.11	A

The compositional fluctuations as well as the Na and K excess values of all analyzed GBs of the absorber are summarized in Table I. In general, we observe that the GBs in the absorber are decorated by Na and K atoms with excess values of $\Gamma_{Na} = 0.19-1.27$ atoms/nm^2 and $\Gamma_K = 0.05-0.18$ atoms/nm^2, respectively. The average Na excess is $\bar{\Gamma}_{Na} = 0.49 \pm 0.36$ atoms/nm^2 and hence ten times larger than the value for GBs in the precursor. The average K excess in the absorber is $\bar{\Gamma}_K = 0.13 \pm 0.04$ atoms/nm^2, whereas K is not detectable in the precursor. The strong variations in the Gibbsian interfacial excess values of Na may be ascribed to variations in GB misorientation and character [30]. Regarding the matrix elements, we observe slight fluctuations at several GBs. However, they are less pronounced as compared to the fluctuations at precursor GBs. For Cu we detect no general trend, as we observe both enrichment and depletion at GBs. Zn and Sn tend to be slightly depleted at GBs, if there is any fluctuation. In contrast, Se is slightly enriched at several GBs.

C. Chemical fluctuations at stacking faults and dislocations

We also detect fluctuations of the matrix elements and impurities at confined two-dimensional and line-shaped features, which are most likely stacking faults (SF) and dislocations [31,32], respectively (see Supplemental Material [48] for how to distinguish GBs from SFs). Figures 4(a) and 4(b) shows an APT dataset of the Cu-poor precursor. Gray isocomposition surfaces corresponding to 20 at.% Zn mark two SFs (I and II), whereas the blue isocomposition surfaces of 26 at.% Cu mark a dislocation (III). The relative composition fluctuations of Cu, Zn, and Sn across the SF I [shown in Fig. 4(c)] reveals a Zn composition twice as high compared to the grain interior, as well as a clear Cu and Sn depletion. We detect neither any

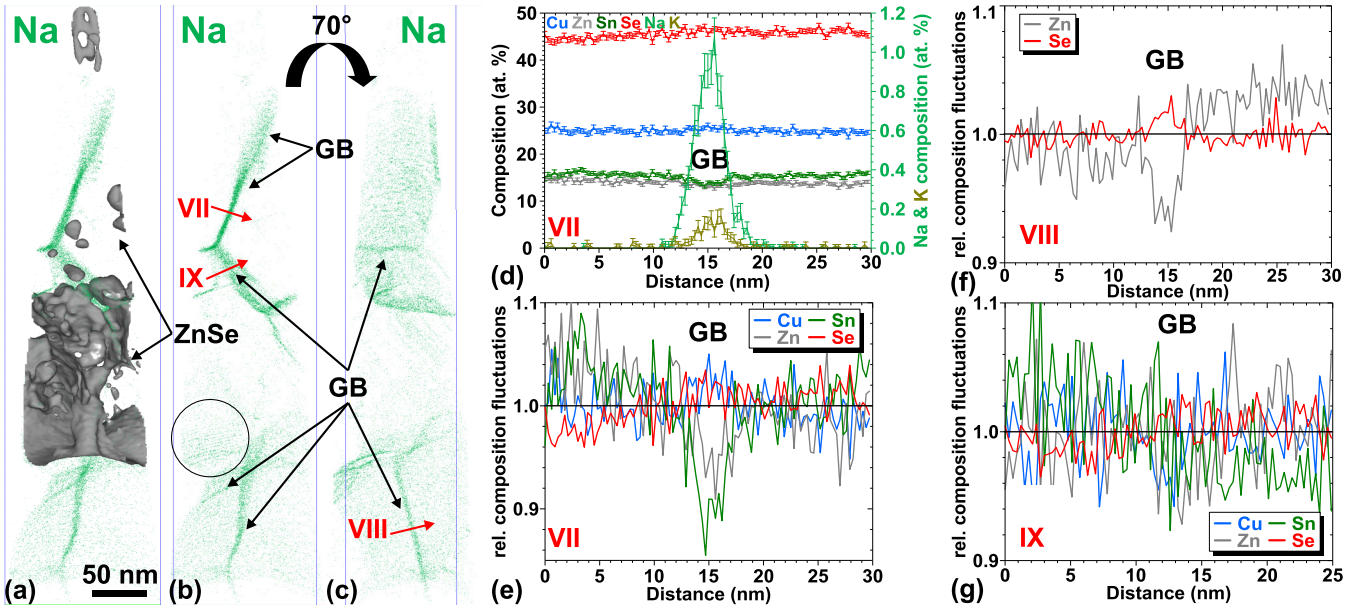

FIG. 3. (a)–(c) Three-dimensional elemental maps of Na (green) atoms from a dataset of the Cu-poor absorber. (c) is rotated by 70° with respect to (a) and (b). The gray isocomposition surfaces in (a) mark 32.0 at.% Zn and, hence, ZnSe precipitates. (d) The composition profiles across the GBs VII, i.e., along the red arrow given in (b). (e)–(g) The calculated relative composition fluctuations across the GBs VII–IX, i.e., along the red arrows given in (b) and (c). (b) Shows additionally by a circle marked area, where Na is enriched at dislocations that are located along a ZnSe/CZTSe interface (see text for more details). For rotating elemental maps, see the Supplemental Material [48].

Se fluctuation nor any impurity segregation at the SF. The second SF II in Figs. 4(a) and 4(b) shows the same trend as SF I. For the dislocation III, we detect compositional fluctuations as shown in Fig. 4(d). We measure a clear enrichment of Cu and depletion of Sn as well as a slight Se depletion, whereas we do not detect any fluctuation of the Zn composition. We also detect Na segregation of approximately 0.05 at.% (not shown here) at the dislocation.

In the absorber, we detect several line-shaped Na segregation zones, most likely being dislocations [see Figs. 5(a) and 5(b)]. For the dislocations V and VI given in Figs. 5(a) and 5(b), the Na compositions are approximately 0.25 at.% and 0.15 at.%, respectively. Co-segregation of K is not observed. The relative composition fluctuation profiles across both dislocations V and VI, shown in Figs. 5(c) and 5(d) exhibit different chemical fluctuations. For dislocation V, we detect Cu depletion and a slight enrichment of Se, whereas for the other dislocation VI, we find Zn depletion as well as Sn enrichment. The other matrix elements show no fluctuation across the dislocation lines. At three other dislocations of a dataset from the same Cu-poor absorber, we do not observe any composition variation of the matrix elements (see Supplemental Material [48]).

Similar to the precursor, we also find in the absorber some Na clusters [see Figs. 5(a) and 5(b)], where the Na composition varies between 1.2 at.% and 2.5 at.%.

The compositional fluctuations of the matrix elements and the Na and K compositions of all analyzed stacking fault and dislocations of the precursor and absorber sample are summarized in Table II.

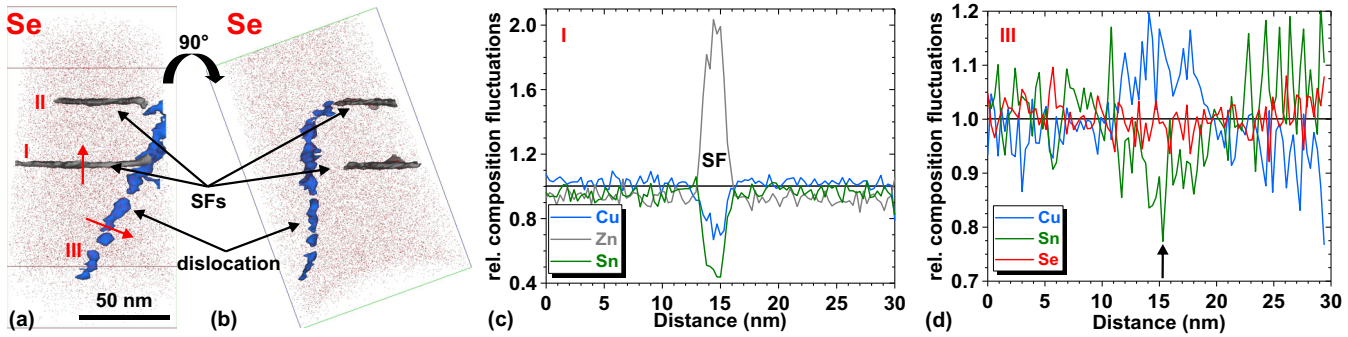

FIG. 4. (a), (b) APT dataset from the Cu-poor precursor. (b) is rotated by 90° with respect to (a). The gray and blue isocomposition surfaces in (a) and (b) mark 20.0 at.% Zn and 26 at.% Cu, respectively Two stacking faults (I and II) and a dislocation (III) are observed. (c), (d) Relative composition fluctuation profiles across the stacking fault I and the dislocation III, i.e., along the red arrows given in (b). The black arrow in (d) marks the position of the dislocation.

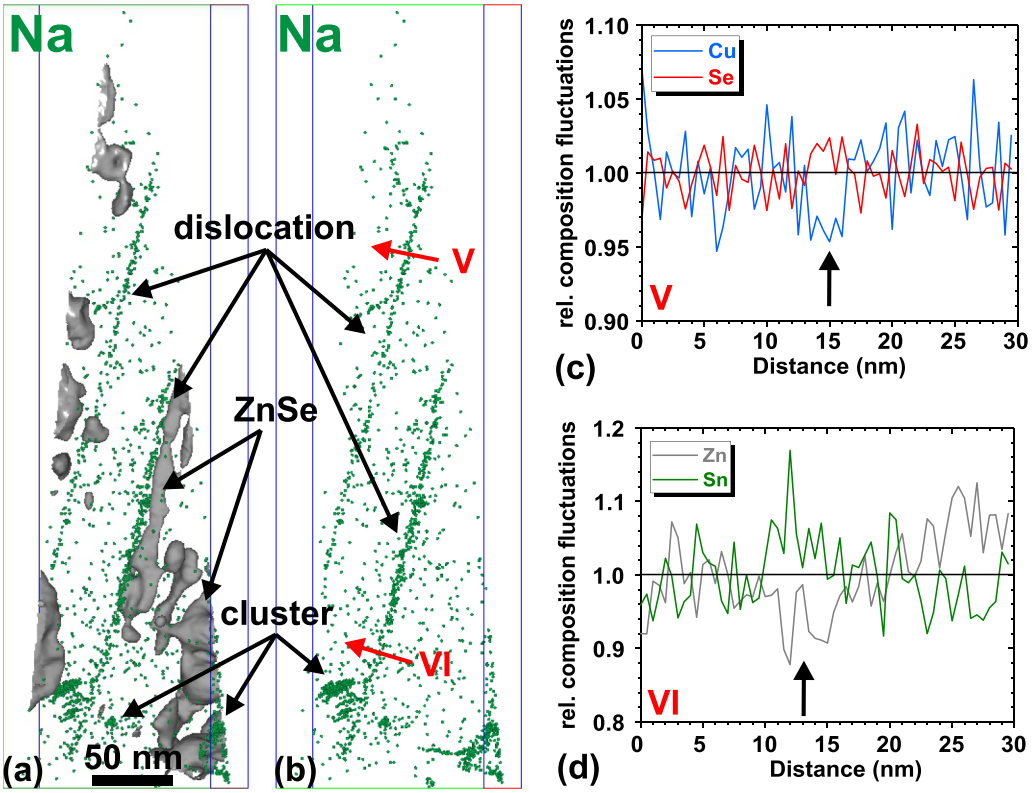

FIG. 5. (a), (b) Three-dimensional elemental maps of Na (green) atoms from an APT dataset of the Cu-poor absorber. The gray isocomposition surfaces in (a) mark 32.0 at.% Zn and, hence, ZnSe precipitates. (c), (d) The relative composition fluctuation profiles across the dislocations I and II, i.e., along the red arrows given in (b). The black arrows in (c) and (d) mark the position of the dislocations. For elemental maps viewed from different perspectives, see the Supplemental Material [48].

IV. DISCUSSION

In this work, we confirmed that the GBs in Cu-poor CZTSe films exhibit different compositional trends before and after annealing at 500 °C (i.e., precursor vs absorber). First, the average Na excess at GBs in the precursor sample with $\overline{\Gamma_{Na}} = 0.05$ atoms/nm^2 is ten times smaller than in the absorber sample. Segregation of Na at GBs at deposition temperatures as low as 320 °C has not yet been observed in CZTS(e). Second, we also detect composition variations of the matrix elements at GBs in the annealed Cu-poor absorber film, in contrast to our previous study where we did not detect such fluctuations at Na-decorated GBs [14]. While GBs in the precursor are generally strongly Cu enriched and Zn depleted, the absorber shows much less compositional variation at GBs. The annealing has led to a homogenization of the composition. In particular, it did remove the strong Cu enrichment at GBs, which is likely to lead to highly conductive GBs, which shortcut the device.

TABLE II. Chemical composition changes of the matrix elements at CZTSe stacking faults and dislocations. +, −, o correspond to enrichment, depletion, and no change, respectively. SF, DL, P, and A stand for stacking fault, dislocation, precursor, and absorber, respectively.

Defect	Cu	Zn	Sn	Se	Na (at.%)	K (at.%)	Sample
SF I	−−	++	−−	o	−	−	P
SF II	−−	++	−−	o	−	−	P
DL III	+	o	−	−	0.05	−	P
DL IV	o	o	o	o	1.20	−	P
DL V	−	o	o	+	0.25	−	A
DL VI	o	−	+	o	0.15	−	A
DL VII	o	o	o	o	0.45	0.10	A
DL VIII	o	o	o	o	0.20	−	A
DL IX	o	o	o	o	0.75	−	A

Similar observations have been made for other structural defects, i.e., stacking faults and dislocations. While the precursor contained strongly Cu-depleted stacking faults, they were not detected in the annealed film. Most dislocations found in the annealed film did not show any composition variations. Thus, the annealing step seems to lead to a reduced stacking fault density and to a strong reduction of compositional fluctuations. This will lead to reduced tail states [33] and, thus, to an absorber film yielding working solar cells. It can be concluded that a high-temperature annealing step is needed to provide absorber material with sufficient homogeneity to allow the preparation of solar cells.

The observed Na and K segregation at defects can be ascribed to out-diffusion of Na and K atoms from the SLG substrate. In the precursor, the average Na composition at GBs is about one order of magnitude smaller than at GBs in the absorber, and in the absorber, it is about four times larger than the K composition at GBs. Taking into account that there are about 14 at.% of Na_2O and only about 0.4 at.% of K_2O in

the SLG substrate, our results suggest that the diffusivity of Na and K are similar, although the ionic radius of K, being 133 pm, is larger than that of Na, which is 98 pm [34]. This is confirmed by the studies of Laemmle *et al.* [35] and Schwarz *et al.* [36], who observed similar findings for the K and Na diffusion in Cu(In, Ga)Se_2.

The enhanced segregation of solutes at GBs in the absorber could be the cause for the observed change in GB composition after the postdeposition annealing. Density functional theory (DFT) calculations by Liu *et al.* [37] suggest that segregation of Na atoms at a $\Sigma 3$ (114) GB can reduce the energy of the GB even further compared to segregation of Cu atoms. Hence, Na atoms substitute Cu atoms from Cu-enriched GBs during the annealing process. For the precursor, this mechanism could be suppressed due to the low deposition temperature (320 °C), which leads to a small Na diffusivity. The works of Bag *et al.* [10] and Wang *et al.* [11] support our findings regarding the substitution of Cu with Na since they detected, by using STEM-EDX, Cu-enriched but no Cu-depleted GBs in Cu-poor and Zn-rich CZTSSe absorbers deposited on a Mo-coated SLG substrate. Although a short annealing of 5 min at 540 °C was applied in their work, the kinetics do not seem to be sufficient to reduce the Cu content at GBs via the substitution with Na.

Furthermore, GBs in the absorber in our study having an Na excess of $\Gamma_{Na} > 1\,\text{atoms/nm}^2$ (see Table I) are not homogeneously decorated by Na (see Fig. S4 in the Supplemental Material [48]). For such high excess values, the interaction between solutes, i.e., Na atoms, has to be taken into account for the segregation phenomena at GBs [38]. Here, the interaction between Na atoms is attractive, leading to a clustering of Na atoms within the GB plane.

Na and K dopants in the CZTSe bulk and their segregation at defects in the absorber can be beneficial for solar-cell performance. Prabhakar *et al.* [39] showed that Na increases the hole composition and conductivity of Cu-poor CZTS films. Na was also reported to increase the open-circuit voltage V_{OC}, fill factor FF, as well as the short-circuit current J_{SC} in Cu-poor and Zn-rich CZTS(e) films [40,41]. According to Yin *et al.* [42], Na can lead to a downward bending of the conduction-band minimum (CBM) and valence-band maximum (VBM) at GBs. Such a mechanism would cause the formation of a hole barrier, which may partially passivate GBs due to a reduced recombination of holes with photogenerated electrons. For CZTSe, the VBM is given by the Se-Cu *p-d* hybridization and, hence, by the Cu composition [43,44]. Therefore, the passivation effect of Na might be enhanced or diminished by the slight Cu depletion or enrichment, which we detect at GBs and dislocations in the absorber film in this work. Also, Bag *et al.* [10] suggests that the lack of Cu-depleted GBs might be a main origin for the observed reduced V_{OC} in their devices.

For K, similar effects on the cell properties as for Na has been described, namely, an increase in V_{OC}, FF, and J_{SC} [45–47]. However, according to Haass *et al.* [46], the beneficial effect of K occurs only for compositions lower than ~0.1 at.% due to the formation of $Sn(S, Se)_2$ upon further increased K composition. In our study, we neither measure K compositions exceeding this critical value [cf. Fig. 3(d)] nor detect $SnSe_2$. Thus, K is expected to have a beneficial effect on the cell efficiency for the studied absorber.

V. CONCLUSIONS

In this work, we performed APT studies on extended defects in Cu-poor and Zn-rich CZTSe films and showed that not only GBs but also SFs and dislocations can be chemically versatile.

We observed that out-diffusion of Na from the soda-lime glass substrate and segregation of Na at GBs and dislocations already take place in a low-temperature (320 °C) grown precursor film. The GBs in the precursor film exhibit Cu enrichments and depletion of Zn, Sn, and Se. After annealing the precursor at 500 °C for 30 min, we detected an increase in the Gibbsian interfacial excess of Na at GBs by one order of magnitude as compared to the precursor. Besides segregation of impurities, we could detect slight composition fluctuations of the matrix elements at some GBs and dislocations for the annealed CZTSe film. For GBs showing chemical fluctuations, we detected Zn and Sn depletion and Se enrichment, whereas there was no clear trend for Cu. While dislocations showed no clear compositional trends, SFs detected in the precursor film showed clear Zn enrichment as well as Cu and Sn depletion. No segregation of impurities was detected at SFs. The annealing did reduce all observed chemical fluctuations.

ACKNOWLEDGMENTS

The authors are grateful to Uwe Tezins and Andreas Sturm for their support to the APT, SEM, and FIB facilities at Max-Planck-Institut für Eisenforschung GmbH. This work was supported by the German Research Foundation (DFG) (Contract No. GA 2450/1-1) and by the Luxembourgish Fonds National de la Recherche. P.C. also acknowledges funding from the National Research Foundation of Korea (NRF) (Grant No. 2016R1A2B4012426).

[1] S. K. Wallace, D. B. Mitzi, and A. Walsh, The steady rise of kesterite solar cells, ACS Energy Lett. **2**, 776 (2017).

[2] X. Liu, Y. Feng, H. Cui, F. Liu, X. Hao, G. Conibeer, D. B. Mitzi, and M. Green, The current status and future prospects of kesterite solar cells: A brief review, Prog. Photovoltaics Res. Appl. **24**, 879 (2016).

[3] S. Siebentritt and S. Schorr, Kesterites - a challenging material for solar cells, Prog. Photovoltaics **20**, 512 (2012).

[4] W. Wang, M. T. Winkler, O. Gunawan, T. Gokmen, T. K. Todorov, Y. Zhu, and D. B. Mitzi, Device characteristics of CZTSSe thin-film solar cells with 12.6% efficiency, Adv. Energy Mater. **4**, 1301465 (2014).

[5] DGIST, PVSEC-36 conference, certified by KIER, 2016 (unpublished).
[6] R. Scheer and H. W. Schock, *Chalcogenide Photovoltaics: Physics, Technologies, and Thin Film Devices* (Wiley-VCH Verlag GmbH, Weinheim, 2011).
[7] W. K. Metzger and M. Gloeckler, The impact of charged grain boundaries on thin-film solar cells and characterization, J. Appl. Phys. **98**, 063701 (2005).
[8] J.-S. Park, S. Kim, and A. Walsh, Opposing effects of stacking faults and antisite domain boundaries on the conduction band edge in kesterite quaternary semiconductors, Phys. Rev. Mater. **2**, 014602 (2018).
[9] C. Donolato, Modeling the effect of dislocations on the minority carrier diffusion length of a semiconductor, J. Appl. Phys. **84**, 2656 (1998).
[10] S. Bag, O. Gunawan, T. Gokmen, Y. Zhu, T. K. Todorov, and D. B. Mitzi, Low band gap liquid-processed CZTSe solar cell with 10.1% efficiency, Energy Environ. Sci. **5**, 7060 (2012).
[11] K. Wang, B. Shin, K. B. Reuter, T. Todorov, D. B. Mitzi, and S. Guha, Structural and elemental characterization of high efficiency Cu_2ZnSnS_4 solar cells, Appl. Phys. Lett. **98**, 051912 (2011).
[12] T. Thersleff, S. Giraldo, M. Neuschitzer, P. Pistor, E. Saucedo, and K. Leifer, Chemically and morphologically distinct grain boundaries in Ge-doped $Cu_2ZnSnSe_4$ solar cells revealed with STEM-EELS, Mater. Des. **122**, 102 (2017).
[13] S.-H. Wu, C.-W. Chang, H.-J. Chen, C.-F. Shih, Y.-Y. Wang, C.-C. Li, and S.-W. Chan, High-efficiency $Cu_2ZnSn(S, Se)_4$ solar cells fabricated through a low-cost solution process and a two-step heat treatment, Prog. Photovoltaics Res. Appl. **25**, 58 (2017).
[14] T. Schwarz, O. Cojocaru-Miredin, P. Choi, M. Mousel, A. Redinger, S. Siebentritt, and D. Raabe, Atom probe tomography study of internal interfaces in $Cu_2ZnSnSe_4$ thin-films, J. Appl. Phys. **118**, 095302 (2015).
[15] S. Tajima, R. Asahi, D. Isheim, D. N. Seidman, T. Itoh, and K.-i. Ohishi, Sodium distribution in solar-grade Cu_2ZnSnS_4 layers using atom-probe tomographic technique, Japan J. Appl. Phys. **54**, 112302 (2015).
[16] T. Schwarz, O. Cojocaru-Miredin, P. Choi, M. Mousel, A. Redinger, S. Siebentritt, and D. Raabe, Atom probe study of $Cu_2ZnSnSe_4$ thin-films prepared by co-evaporation and post-deposition annealing, Appl. Phys. Lett. **102**, 042101 (2013).
[17] S. Tajima, R. Asahi, D. Isheim, D. N. Seidman, T. Itoh, M. Hasegawa, and K. Ohishi, Atom-probe tomographic study of interfaces of Cu_2ZnSnS_4 photovoltaic cells, Appl. Phys. Lett. **105**, 093901 (2014).
[18] S. Chen, A. Walsh, X. G. Gong, and S. H. Wei, Classification of lattice defects in the kesterite Cu_2ZnSnS_4 and $Cu_2ZnSnSe_4$ earth-abundant solar cell absorbers, Adv. Mater. **25**, 1522 (2013).
[19] T. Todorov, J. Olenick, K. Aolenick, O. Gunawan, T. Gershon, C. Sturdevant, L. Yun Seog, C. Liang-yi, and S. Guha, Flexible kesterite solar cells on ceramic substrates for advanced thermal processing, in *2015 IEEE 42nd Photovoltaic Specialist Conference (PVSC)* (IEEE, 2015), pp. 1–3.
[20] S. G. Haass, M. Diethelm, M. Werner, B. Bissig, Y. E. Romanyuk, and A. N. Tiwari, 11.2% efficient solution processed kesterite solar cell with a low voltage deficit, Adv. Energy Mater. **5**, 1500712 (2015).
[21] Y. S. Lee, T. Gershon, O. Gunawan, T. K. Todorov, T. Gokmen, Y. Virgus, and S. Guha, $Cu_2ZnSnSe_4$ thin-film solar cells by thermal co-evaporation with 11.6% efficiency and improved minority carrier diffusion length, Adv. Energy Mater. **5**, 1401372 (2015).
[22] K. Shinho, K. Kang Min, T. Hitoshi, S. Hajime, and N. Shigeru, Improvement of voltage deficit of Ge-incorporated kesterite solar cell with 12.3% conversion efficiency, Appl. Phys. Express **9**, 102301 (2016).
[23] M. Mousel, T. Schwarz, R. Djemour, T. P. Weiss, J. Sendler, J. C. Malaquias, A. Redinger, O. Cojocaru-Miredin, P. P. Choi, and S. Siebentritt, Cu-rich precursors improve kesterite solar cells, Adv. Energy Mater. **4**, 1300543 (2014).
[24] K. Thompson, D. Lawrence, D. J. Larson, J. D. Olson, T. F. Kelly, and B. Gorman, *In situ* site-specific specimen preparation for atom probe tomography, Ultramicroscopy **107**, 131 (2007).
[25] J. Timo Wätjen, J. J. Scragg, M. Edoff, S. Rubino, and C. Platzer-Björkman, Cu out-diffusion in kesterites—A transmission electron microscopy specimen preparation artifact, Appl. Phys. Lett. **102**, 051902 (2013).
[26] Y. S. Yee, B. Magyari-Köpe, Y. Nishi, S. F. Bent, and B. M. Clemens, Deep recombination centers in $Cu_2ZnSnSe_4$ revealed by screened-exchange hybrid density functional theory, Phys. Rev. B **92**, 195201 (2015).
[27] A. Redinger, M. Mousel, M. H. Wolter, N. Valle, and S. Siebentritt, Influence of S/Se ratio on series resistance and on dominant recombination pathway in $Cu_2ZnSn(SSe)_4$ thin film solar cells, Thin Solid Films **535**, 291 (2013).
[28] O. C. Hellman and D. N. Seidman, Measurement of the Gibbsian interfacial excess of solute at an interface of arbitrary geometry using three-dimensional atom probe microscopy, Mater. Sci. Eng.: A **327**, 24 (2002).
[29] W.-C. Hsu, I. Repins, C. Beall, C. DeHart, G. Teeter, B. To, Y. Yang, and R. Noufi, The effect of Zn excess on kesterite solar cells, Sol. Energy Mater. Sol. Cells **113**, 160 (2013).
[30] M. Herbig, D. Raabe, Y. J. Li, P. Choi, S. Zaefferer, and S. Goto, Atomic-Scale Quantification of Grain Boundary Segregation in Nanocrystalline Material, Phys. Rev. Lett. **112**, 126103 (2014).
[31] O. Cojocaru-Mirédin, T. Schwarz, and D. Abou-Ras, Assessment of elemental distributions at line and planar defects in $Cu(In,Ga)Se_2$ thin films by atom probe tomography, Scr. Mater. **148**, 106 (2017).
[32] G. D. W. Smith, D. Hudson, P. D. Styman, and C. A. Williams, Studies of dislocations by field ion microscopy and atom probe tomography, Philos. Mag. **93**, 3726 (2013).
[33] S. Siebentritt, G. Rey, A. Finger, D. Regesch, J. Sendler, T. P. Weiss, and T. Bertram, What is the bandgap of kesterite? Sol. Energy Mater. Sol. Cells **158**, 126 (2016).
[34] H. Francois-Saint-Cyr, E. Anoshkina, F. Stevie, L. Chow, K. Richardson, and D. Zhou, Secondary ion mass spectrometry characterization of the diffusion properties of 17 elements implanted into silicon, J. Vac. Sci. Technol. B: Microelectron. Nanometer Struct. **19**, 1769 (2001).
[35] A. Laemmle, Dotierung von $Cu(In,Ga)Se_2$-Schichten mit Natrium und Kalium zur Steigerung des Wirkungsgrads, Ph.D. thesis, Karlsruher Institut für Technologie (KIT), 2015.
[36] T. Schwarz, G. Stechmann, B. Gault, O. Cojocaru-Mirédin, R. Wuerz, and D. Raabe, Correlative transmission Kikuchi

diffraction and atom probe tomography study of Cu(In,Ga)Se_2 grain boundaries, Prog. Photovoltaics Res. Appl. **26**, 196 (2018).

[37] C.-Y. Liu, Z.-M. Li, H.-Y. Gu, S.-Y. Chen, H. Xiang, and X.-G. Gong, Sodium passivation of the grain boundaries in $CuInSe_2$ and Cu_2ZnSnS_4 for high-efficiency solar cells, Adv. Energy Mater. **7**, 1601457 (2017).

[38] P. Lejcek, *Grain Boundary Segregation in Metals* (Springer-Verlag, Berlin, 2010).

[39] T. Prabhakar and N. Jampana, Effect of sodium diffusion on the structural and electrical properties of Cu_2ZnSnS_4 thin films, Sol. Energy Mater. Sol. Cells **95**, 1001 (2011).

[40] H. Zhou, T. B. Song, W. C. Hsu, S. Luo, S. Ye, H. S. Duan, C. J. Hsu, W. Yang, and Y. Yang, Rational defect passivation of $Cu_2ZnSn(S,Se)_4$ photovoltaics with solution-processed Cu_2ZnSnS_4:Na nanocrystals, J. Am Chem. Soc. **135**, 15998 (2013).

[41] I. Repins, C. Beall, N. Vora, C. DeHart, D. Kuciauskas, P. Dippo, B. To, J. Mann, W.-C. Hsu, A. Goodrich, and R. Noufi, Co-evaporated $Cu_2ZnSnSe_4$ films and devices, Sol. Energy Mater Sol. Cells **101**, 154 (2012).

[42] W.-J. Yin, Y. Wu, S.-H. Wei, R. Noufi, M. M. Al-Jassim, and Y. Yan, Engineering grain boundaries in $Cu_2ZnSnSe_4$ for better cell performance: A first-principles study, Adv. Energy Mater. **4**, 1300712 (2014).

[43] S. Chen, X. G. Gong, A. Walsh, and S.-H. Wei, Crystal and electronic band structure of Cu_2ZnSnX_4 (X = S and Se) photovoltaic absorbers: First-principles insights, Appl. Phys. Lett. **94**, 041903 (2009).

[44] J. Paier, R. Asahi, A. Nagoya, and G. Kresse, Cu_2ZnSnS_4 as a potential photovoltaic material: A hybrid Hartree-Fock density functional theory study, Phys. Rev. B **79**, 115126 (2009).

[45] W. Li, Z. Su, J. M. R. Tan, S. Y. Chiam, H. L. Seng, S. Magdassi, and L. H. Wong, Revealing the role of potassium treatment in CZTSSe thin film solar cells, Chem. Mater. **29**, 4273 (2017).

[46] S. G. Haass, C. Andres, R. Figi, C. Schreiner, M. Bürki, A. N. Tiwari, and Y. E. Romanyuk, Effects of potassium on kesterite solar cells: Similarities, differences and synergies with sodium, AIP Adv. **8**, 015133 (2018).

[47] G. Rey, F. Babbe, T. P. Weiss, H. Elanzeery, M. Melchiorre, N. Valle, B. E. Adib, and S. Siebentritt, Post-deposition treatment of $Cu_2ZnSnSe_4$ with alkalis, Thin Solid Films **633**, 162 (2017).

[48] See Supplemental Material at http://link.aps.org/supplemental/10.1103/PhysRevMaterials.3.035402 for Na segregation at dislocations at the ZnSe/CZTSe interface, Na segregation at a dislocation loop, inhomogeneous Na segregation at a CZTSe GB, and rotating 3D elemental APT maps.